Title
Towards Accurate Broadband Noise Predictions Using CFD

Journal
Proceedings of the Vertical Flight Society 79th Annual Forum and Technology Display

Authors
Won, Jordon

Trembois, Nikos

Lee, Seongkyu

Publication Date
2023-05-16

DOI
10.4050/f-0079-2023-17950

Towards Accurate Broadband Noise Predictions Using CFD

Jordon Won
PhD Candidate
University of California
Davis, California, USA

Nikos Trembois
PhD Candidate
University of California
Davis, California, USA

Seongkyu Lee
Associate Professor
University of California
Davis, California, USA

ABSTRACT

Rotor broadband noise can be predicted using various numerical and analytical methods. This paper explores the application of computational fluid dynamics (CFD) combined with Lee's wall pressure spectrum and Amiet's trailing edge noise model to predict broadband noise, comparing the results to different experiments. A simple, ideally twisted rotor blade with the NACA 0012 airfoil in hover is employed to establish the appropriate methodology for integrating CFD with other models. Two approaches are utilized: the first is a direct input approach, where flow data from the CFD solution is directly input into the models, while the second approach employs CFD to inform XFOIL inputs, which subsequently provide inputs for the wall pressure spectrum and acoustic model. The CFD/XFOIL approach demonstrates better agreement with experimental measurements and is less sensitive to CFD pre- and post-processing setups. The Straight Up Imagining (SUI) Endurance rotor is also validated for forward flight, followed by the prediction of broadband noise generated by a propeller and wing configuration. Observed trends during the validations and predictions suggest that airfoil selection and blade geometry play a more significant role in the magnitude of trailing edge noise than thrust.

INTRODUCTION

In recent years, there has been a growing interest in rotorcraft acoustics in urban cities due to the increasing prevalence of drones and the development of urban air mobility (UAM) vehicles. With drones becoming readily accessible for both recreational and professional use, noise pollution has become a significant concern, with Schaffer *et al.* (Ref. 1) noting that this type of noise is particularly annoying compared to that generated by jets and automobiles. Similarly, UAM vehicles are expected to contribute further to noise pollution, with high annoyance levels. Overall, noise remains a significant issue that limits the widespread adoption of these rotorcraft. Similar to how airports are required to mitigate noise pollution, Kim (Ref. 2) discussed the need to address UAM noise to avoid disturbing urban populations. Greenwood *et al.* (Ref. 3) provided a thorough review of UAM noise, and Sarojini *et al.* (Ref. 4) incorporated UAM aircraft noise into their multidisciplinary aircaft design and optimization study. Additionally, Orndorff *et al.* took UAM noise into consideration in their flight optimization research (Ref. 5).

The importance of aerodynamic noise has led to extensive research into modeling and predicting rotor noise. Noise can be categorized as low to mid-frequency tonal noise or high-frequency broadband noise. Since human hearing is sensitive to high-frequency noise, there have been recent investigations into broadband noise. Research conducted by Brooks *et al.* (Ref. 6) identified five mechanisms that can cause airfoil-self broadband noise, with turbulent boundary-layer trailing-edge noise being a dominant contributor. Trailing-edge noise arises when turbulent flow passes over the trailing edge of an airfoil, causing pressure fluctuations from the turbulence to scatter and produce acoustic energy. Lee *et al.* (Ref. 7) presented the current methods for predicting trailing-edge noise in a comprehensive review paper. These methods include analytical and empirical models, as well as numerical and experimental approaches. Some analytical models highlighted were those by Wiener and Hopf, Amiet, and Howe (Refs. 8–10). The advantage of using these models is that they are based on fundamental physics.

The Amiet model, which has been modified according to the suggestions made by Roger and Moreau (Ref. 11) and Li and Lee (Ref. 12), is of particular interest in this paper, as it predicts trailing-edge noise based on the pressure spectrum on the surface near the trailing edge. It is important to note that the pressure spectrum reflects the flow characteristics and can be related to boundary layer properties. Therefore, it can be obtained through either measurement or computation, given a flow field. It should be noted that the prediction of the pressure spectrum is separate from the acoustic model, so it is assumed that the scattering of pressure by the trailing edge does not affect the pressure spectrum.

Current models used to predict the pressure spectrum at the surface are often derived empirically or semi-empirically. An empirical model developed by Goody (Ref. 13) provided good agreement with measurements for zero pressure gradient flows, such as those over a flat plate, but was inadequate for airfoils with significant pressure gradients. To account for pressure gradients, several empirical or semi-empirical

Presented at the Vertical Flight Society 79th Annual Forum & Technology Display, West Palm Beach, Florida, May 16–18, 2023.

models were developed (see a comprehensive review paper about the empirical wall pressure spectrum models by Lee (Ref. 14)). Lee developed a new empirical wall pressure spectrum model, named Lee's model. As previously mentioned, the pressure spectrum is characterized by the boundary layer near the trailing edge. Thus, relevant parameters obtained from the flow field to calculate the wall pressure spectrum include boundary layer thickness, displacement thickness, momentum thickness, edge velocity, pressure gradient, and skin friction. These parameters can be obtained from XFOIL or steady Reynolds Averaged Navier-Stokes (RANS) solvers. When predicting trailing-edge noise, Lee's model performed better than previously developed models for a variety of cases (Ref. 15).

Other semi-empirical models have been developed for acoustic prediction, with the most popular being the Brooks, Pope, and Marcolini (BPM) model (Ref. 16). Unlike the previously discussed models, the BPM model does not require a wall pressure spectrum as an input but still relies on boundary layer parameters, such as displacement thickness. The model was based on theoretical results that were tuned using experiments on a NACA 0012 airfoil. Thus, there are concerns regarding the validity of this model as it was only tuned to match measurements from a specific airfoil. Moreover, since the prediction of self-noise, such as trailing-edge noise, is primarily based on a single parameter, that is the displacement thickness, it is questionable how well the model can account for different flow fields with arbitrary cambered airfoils. For more detailed discussions on the validity and issue of the BPM model, refer to a reference (Ref. 7).

Semi-empirical and analytical models are considered low to moderate fidelity prediction methods. High fidelity approaches involve modeling all the turbulence near the surface of an airfoil, which requires high fidelity Large Eddy Simulation (LES) (Refs. 17, 18). However, using full LES methods for predicting noise at a given observer location is prohibitively expensive. To overcome this challenge, hybrid methods are used, which combine LES around the airfoil to capture an accurate description of the turbulence, followed by an acoustic model to determine how noise will propagate given the turbulence.

These different methods for predicting broadband noise have been widely used and are extensively discussed in the literature (Refs. 7, 9, 19). Whelchel *et al.* (Ref. 20) compared their experimental measurements of propellers to low-fidelity aerodynamic prediction tools such as blade element momentum theory (BEMT) and found good agreement for some cases. However, they also noted the limitations of these methods, which motivated the use of higher-fidelity tools such as computational fluid dynamics (CFD) (Refs. 21–25).

Jung et al. (Ref. 21) utilized RANS CFD solutions as inputs for the BPM broadband noise models to investigate the DJI drone rotor. Thurman *et al.* (Ref. 22) studied drone noise using lattice-Boltzmann method-very-large-eddy simulations (LBM-VLES) and the Propeller Analysis System of Aircraft Noise Prediction Program (ANOPP-PAS). Additionally, Thurman *et al.* (Ref. 23) employed LBM-VLES to examine the broadband noise of an ideally twisted rotor blade. Furthermore, Thai *et al.* (Ref. 25) utilized detached eddy simulations (DES) in combination with acoustic models integrated into UCD-QuietFly to predict small-scale rotor trailing-edge noise. Li and Lee (Refs. 19, 26, 27) conducted extensive research on rotor broadband noise using UCD-QuietFly, and most of this work utilized Blade Element Momentum Theory (BEMT) combined with XFOIL. However, a recent version of UCD-QuietFly is compatible with higher fidelity models that use Navier-Stokes equations. Overall, research involving the usage of CFD in rotor broadband noise research has only recently begun, and our comprehension of the accuracy and limitation of CFD-based broadband noise predictions is currently limited. The objective of this paper is to establish the best practices when CFD is employed as input to broadband noise predictions. In addition to CFD-based input, we use Lee's wall pressure spectrum model in a modified Amiet's model in the framework of UCD-QuietFly.

In this study, numerical predictions are compared to experimental results obtained by Pettingill *et al.* on an ideally twisted rotor and the Straight Up Imagining (SUI) Endurance rotor (Refs. 28, 29). The SUI drone is a multi-rotor drone and was tested in forward flight. Additionally, a propeller and wing case was modeled using the Mejzlik propeller to predict how a wing affects the broadband noise produced by a propeller (Ref. 30).

TECHNICAL APPROACH

MODELS

Three distinct cases will be tested in this paper to investigate broadband noise: ideally twisted rotor in hover, SUI endurance drone in forward flight, and Mejzlik propeller with the wing in axial flight. The computed noise levels will be validated against experimental data, except in the last case where no experimental data are available.

Ideally twisted rotor The ideally twisted rotor in this study has four blades with a radius of 158.8 mm and a constant chord length of 31.76 mm (Ref. 28). A single NACA 0012 airfoil is used in the entire blade. The rotor was tested at three different tip angles of 3.9, 6.9, and 9.9 degrees with varying rotation rates from 3000 to 5800 rpm. The baseline case is the blade tip angle of 6.9 degrees at 5500 RPM. Figure 1(a) illustrates the spanwise angle distribution of each rotor blade for the baseline case. The target thrust coefficient using BEMT was 0.0137, but the measured thrust coefficient was 0.0123 for the baseline case. Acoustic data were recorded at five microphone locations for each operating condition as shown in Fig. 1(b), with overall sound pressure level provided at each microphone location and complete sound spectra given only at microphone location five.

SUI rotor The SUI Endurance drone rotor is comprised of two blades, each with a radius of 190.5mm and varying chord

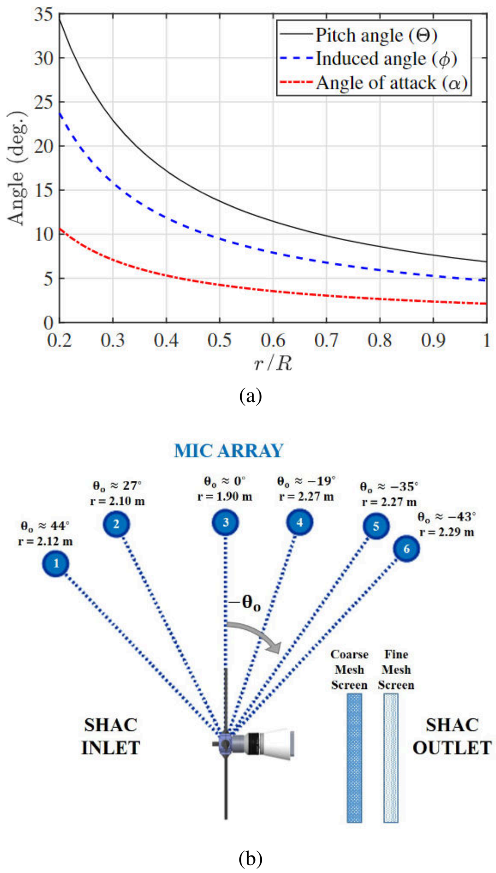

Fig. 1. Ideally twisted rotor: (a) spanwise angle distributions and (b) microphone locations (Ref. 28).

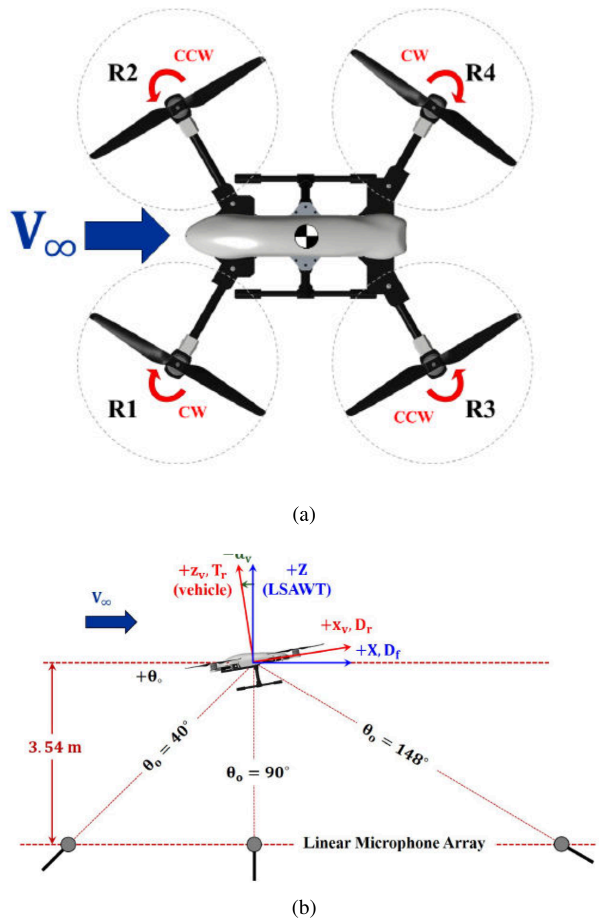

Fig. 2. SUI Endurance drone: (a) CAD geometry of the SUI Endurance drone and (b) LSAWT microphone locations (Ref. 29).

length and airfoil along its span (Ref. 29). Figure 2(a) displays the CAD geometry of the SUI drone. Acoustic measurements for both isolated rotor and rotor with vehicle were conducted and recorded in the NASA Langley Low-Speed Aeroacoustic Wind Tunnel (LSAWT), which has an array of 28 microphones as shown in Fig. 2(b).

For the forward flight cases, the rotors are titled negative 10 degrees about the y-axis. The freestream velocity for this test case was 15.5 m/s, and acoustic measurements were taken for rotor 1 and rotor 3 at the 90-degree location as shown in Fig. 2(b). Rotor 1 had a rotation rate of about 4000 RPM, while rotor 3 rotated at nearly 4900 RPM, producing 10.85 and 15.47 N of thrust, respectively.

Mejzlik propeller with wing Finally, the Mejzlik propeller with wing experiments done by Zawodny *et al.* (Ref. 30) is simulated to predict broadband noise. The measurements were taken on an isolated propeller case and a propeller with wing cases. The placement of the wing relative to the propeller blade's leading edge was varied and can be seen in Fig. 3. The closest wing with $\triangle x/R = 0.25$ and $\triangle z/R = 0.5$ is selected in this paper for the propeller with wing case, where $\triangle x$ and $\triangle z$ are the horizontal and vertical separation distance from the propeller leading edge and from the hub, respectively, and R is the propeller blade radius, as shown in Fig. 3. The propeller has 3 blades with a radius of 200 mm. The wing has a span of 914 mm and a constant chord length of 406 mm. The propeller's airfoil varies along the span, while the wing has a single NACA 63_2-215 airfoil for the entire span. The testing conditions included an advance ratio of 0.592, a tip Mach number of 0.361, and a freestream Mach number of 0.068.

The experiments were conducted in the NACA Langley LSAWT, similar to the SUI rotor. The 90-degree microphone location was used to report the sound pressure level for the isolated propeller, and a linear microphone array was used to show the directivity plot. Only the tonal noise was reported due to interference from other noise sources, which made the broadband measurements unreliable. Therefore, this paper will only present predictions of broadband noise. It is worth noting that Trembois *et al.* (Ref. 31) presented the validation of tonal noise at the first blade passing frequency against the measurement data in a companion paper using the same CFD simulations that are used in the current paper.

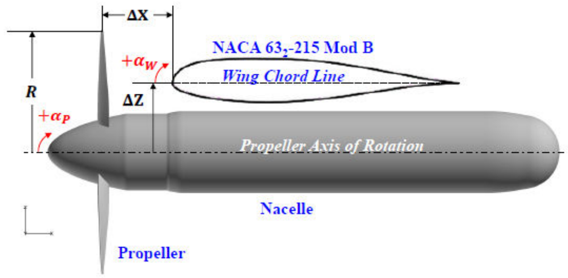

Fig. 3. Mejzlik propeller and wing geometry (Ref. 30).

CFD GRID

The grids used for this paper are generated using the Chimera Grid Tools v2.1 software package and an in-house script that automatically generates structured near-mesh grids (Ref. 32). Figure 4(a) shows the near-body O-type mesh for one of the blades of the ideally twisted rotor. It should be noted that cap meshes for the root and tip of the blade must also be incorporated and overlapped with the main blade mesh to construct a watertight mesh. To investigate the impact of mesh resolution on acoustic predictions, several near-body meshes are evaluated. The first three meshes vary only in the number of grid points in the k-direction, which is normal to the blade, as shown in Fig. 4(a). Following the computation of these three solutions, two additional meshes are analyzed, varying in the i and j-directions in addition to the k-direction. Table 1 provides a detailed description of the near-body mesh. To establish a baseline case, a near-body mesh with 65 grid points in the normal direction is first generated. The near-body mesh is extended to a distance of 1 chord length from the blade. The first cell height is determined by computing a y+ value equivalent to 1 from the tip velocity. For the 5500 RPM scenario, this yields a first cell height of approximately 3.388 x 10^{-6} meters. It is worth noting that the first cell height remains unchanged for the finer meshes, as the only varying parameter is the number of grid points. In addition to the 65 grid points in the normal direction, the baseline mesh consisted of 250 grid points in the i-direction and 150 in the j-direction, representing the circumference of the airfoil and the span of the blade, respectively. It should also be noted that Case 1 in Table 1 corresponds to the baseline mesh.

Table 1. Ideally twisted rotor single blade near-body mesh values.

Case	i	j	k	Near-Body Cells
1	250	150	65	0.98M
2	250	150	128	1.92M
3	250	150	224	8.40M
4	128	100	48	0.25M
5	400	200	128	4.50M

The off-body mesh is generated automatically by OVERFLOW 2.0 using inputs that specify the size of the region and the desired level 1 refinement. The level 1 refinement region denotes the volume where the off-body grid has the smallest cell size. As depicted in Fig. 4(b), cells situated farther from the level 1 refinement region become larger in size. The level 1 refinement region is a rectangle that extends 0.25R beyond the rotor's radius in all directions, except in the negative z-direction, where it stretches 2R to capture the rotor wake. The domain's total size is a 20R-length cube. In most cases tested, the level 1 refinement has a grid spacing of 10% C_{tip} where C_{tip} denotes the chord length at the tip. This yields a level 1 grid spacing of 3.2 mm which results in the off-body mesh containing 18.3 million grid points. Additionally, the baseline near-body mesh, with a 5% C_{tip} grid spacing, is simulated to investigate the impact of off-body mesh resolution on acoustics. The grid spacing for this finer resolution is 1.6 mm yielding an off-body mesh containing 34.5 million grid points.

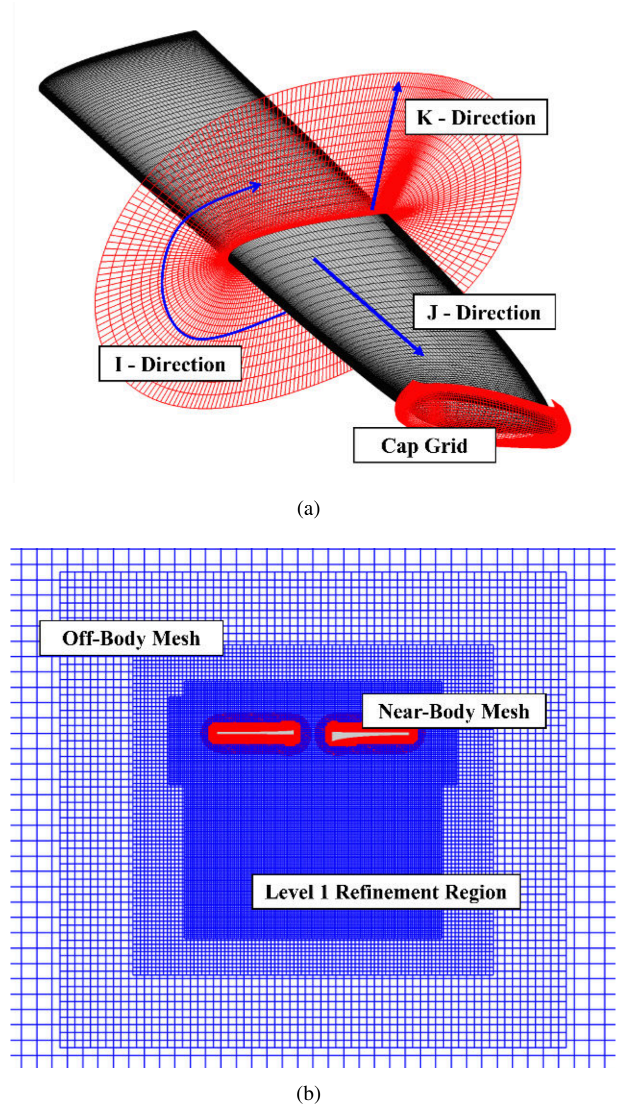

Fig. 4. Ideally twisted rotor grid: (a) near-body O-type mesh and (b) off-body Cartesian mesh

The SUI blade is meshed using the same methodology as the ideally twisted rotor. Figure 5 displays the near-body mesh for a single SUI rotor blade. The SUI blade mesh has 307 grid points in the i-direction, while in the j and k-directions, it has 150 and 168 grid points, respectively. To ensure a y+ value less than 1, the first cell height is set to 3.01 x 10^{-6} m. The total number of cells for the near-body mesh is 24.5 million cells. Additionally, the off-body Cartesian mesh is generated using the same methods as the ideally twisted rotor with 10% C_{tip}. The SUI's off-body mesh consists of 12.4 million grid points with its level 1 grid spacing being 3.5 mm.

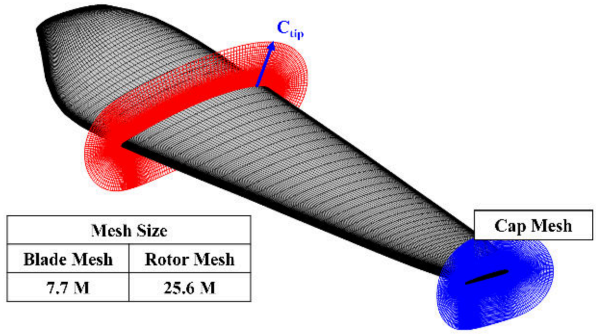

Fig. 5. Near-body surface and volume mesh for a single SUI Endurance drone rotor blade.

A detailed description of the Mejzlik propeller's mesh can be found in Trembois *et al.* (Ref. 31). Each blade comprises 2.54 million grid points, while the wing contains 2.84 million. The near-body mesh contains 24.9 million cells, encompassing the nacelle and all blades. The off-body grid, on the other hand, consists of 15.8 million cells. Figures 6 and 7 show the surface and near-body meshes surrounding the blade and near-body and off-body meshes surrounding the propeller and wing, respectively. (Ref. 31).

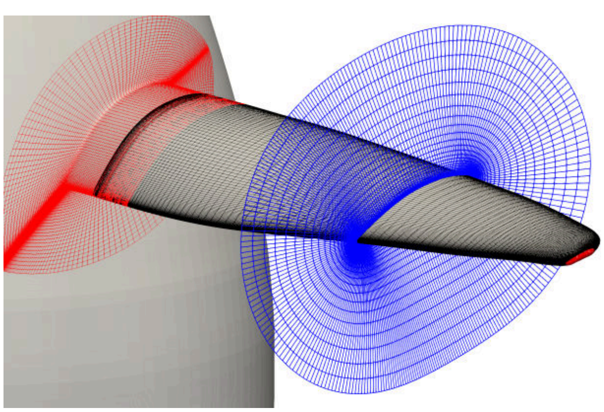

Fig. 6. The blade surface grid with a slice of the near-body volume grids (Ref. 31).

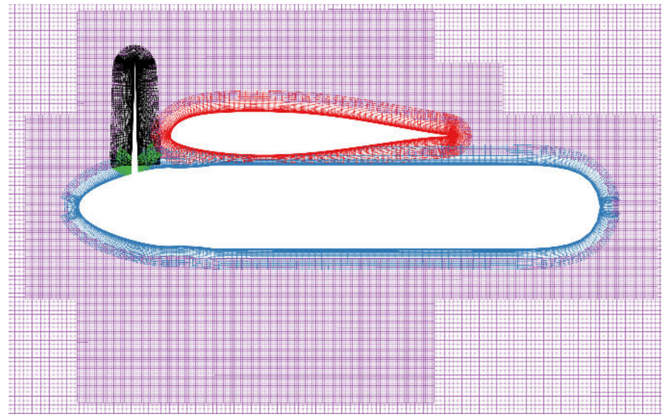

Fig. 7. Near-Body and off-body grids of the Mejzlik propeller with nacelle and wing. (Ref. 31)

CFD SIMULATION

NASA's OVERFLOW (Refs. 33, 34) is used as the CFD tool to solve unsteady compressible Reynolds Averaged Navier-Stokes (RANS) equations. The Spalart-Allmaras (SA) delayed detached eddy simulation (DDES) turbulence model is implemented to capture the detailed vortical eddies in the wake region. Dual time stepping with 40 subiterations is used to advance the simulation by 0.25 azimuthal degrees per physical time step. The second-order backward temporal differencing scheme and fifth-order central spatial scheme for inviscid flux terms are employed.

OVERFLOW has been extensively used in the field of rotor aeroacoustics. For instance, Jia and Lee has recently applied OVERFLOW to study the aeroacoustics of coaxial rotors (Ref. 35), quadrotors (Ref. 36), and side-by-side rotors (Ref. 37). Trembois *et al.* (Ref. 31) used OVERFLOW for the Mejzlik propeller with wing simulations.

AEROACOUSTICS

The UCD-QuietFly v3.0 code (Refs. 12, 19, 26, 27) is used for broadband noise prediction. This code models trailing edge noise using the Amiet model (Ref. 9) in conjunction with the wall pressure spectrum that is obtained from Lee's empirical wall pressure spectrum model (Ref. 14). It was found that Lee's model is superior to other empirical models in terms of trailing-edge noise predictions (Ref. 15). UCD-QuietFly v3.0 is capable of predicting rotor trailing edge noise for both hover and forward flights with single or multi-rotor vehicles. Lee's model, which produces the main input to the Amiet model, is dependent on the boundary layer parameters, such as boundary layer thickness, displacement thickness, momentum thickness, edge velocity, skin friction coefficient, and pressure gradient. This physics-based approach requires more input data than the BPM model. However, having more data ensures a better representation of different flow fields with cambered airfoils.

UCD-QuietFly can obtain boundary layer parameters either by directly using CFD flow data in the boundary layer or by calculating them via XFOIL (Ref. 38). Directly inputting boundary layer parameters requires prior knowledge of their values before the use of UCD-QuietFly. This can be achieved through the post-processing of a CFD solution, where the boundary layer parameters are calculated from the flow variables at each blade section. In contrast, using XFOIL to obtain boundary layer parameters only requires the radial distribution of incoming velocity and angle of attack. UCD-QuietFly is coupled with XFOIL while it is running. The distribution of velocity and angle of attack can be obtained using any aerodynamic model, including blade element momentum theory (BEMT), blade element theory (BET), or CFD indirectly.

This paper utilizes two approaches to predict rotor blade trailing edge noise with CFD. Approach 1 is the direct input approach, where the boundary layer parameters are extracted directly from a CFD solution. This can be done automatically by defining the boundary layer thickness as the point where the turbulent kinetic energy (TKE) or eddy viscosity reaches a minimum threshold as described in Gill and Lee (Ref. 39). Once the boundary layer's edge is located at the 99% chord location along the blade span, parameters like boundary layer thickness, displacement thickness, momentum thickness, edge velocity, friction coefficient, and pressure gradient can be computed at that point. Figure 8(a) illustrates the normalized eddy viscosity and velocity at the r/R = 0.5 section. Eddy viscosity is used because the SA model does not compute TKE. In OVERFLOW, eddy viscosity is divided by dynamic viscosity, and velocity is divided by the speed of sound. Approach 1 provides highly accurate boundary parameters as they are directly extracted from the high-fidelity simulation, enabling it to capture effects that a simple 2D steady solver like XFOIL cannot predict. However, the approach has certain drawbacks: first, inconsistency with the acoustic and wall pressure spectrum models that assume the use of a 2D airfoil, and second, the sensitivity of boundary layer parameters to the method of extraction. The latter is highlighted in Fig. 8(b), where the eddy viscosity exhibits multiple minima near the blade tip. A more in-depth study and detailed discussions will be provided in the results section for the ideally twisted rotor.

Approach 2 is similar to the process developed by Jung *et al.* (Ref. 21). By using the normal, C_n, and chordwise, C_c, force distribution from CFD on each rotor blade, the sectional lift coefficient, C_l, and effective angle of attack, α_e, can be iteratively computed using the following equations:

$$C_l = C_n \cos(\alpha_e) + C_c \sin(\alpha_e) \tag{1}$$

$$C_l = C_{l_\alpha} \alpha_e + C_{l_{\alpha=0^\circ}}, \tag{2}$$

where C_{l_α} represents the lift slope, or 2π, and $C_{l_{\alpha=0^\circ}}$ represents the airfoil's lift coefficient at zero angle of attack. It is important to note that the lift coefficient being computed is the sectional 2D lift coefficient at each modeled radial section, although C_n and C_c are computed by 3-D CFD. The freestream velocity at each section can also be computed by using the rotor's forward velocity and rotation rate, providing all the

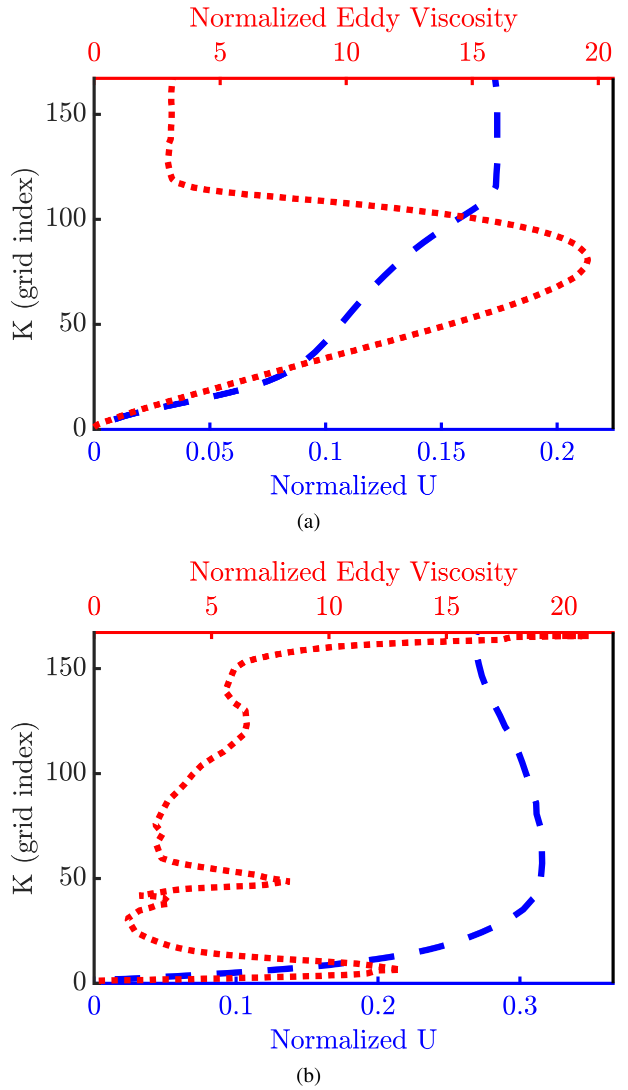

Fig. 8. Near-wall normalized eddy viscosity and velocity values: (a) r/R = 0.5 and (b) r/R = 0.95.

required inputs for XFOIL to calculate the boundary layer parameters. The advantage of this method is that it maintains the 2D airfoil assumption used in UCD-QuietFly's models and is also a less sensitive post-processing method. However, the disadvantage of this method is that the boundary layer values do not directly come from the rotor blade's CFD solution and must be obtained through a different solution using either XFOIL or 2D CFD. Additionally, it is important to note that this method does not account for stall, which is likely to occur near the root section. This is due to the assumption that the airfoil operates in the linear section of its polar. Since the blade root sections rarely contribute to the overall noise level, this assumption is well accepted.

RESULTS

IDEALLY TWISTED ROTOR

In this section, we present the results for an ideally twisted rotor operating at 5500 RPM. Performance outcomes are shown, and both Approach 1 and Approach 2, which were discussed in the technical approach section, are utilized for predicting acoustics.

Performance

Figure 9 shows (a) the normalized vorticity contour in the vertical plane at the rotor center and (b) the normalized iso-surface of Q-criterion with the vorticity colored for the baseline case after 10 revolutions. The Q-criterion shown is 0.1. It is found that the tip and root vortices and the wake sheets are well captured.

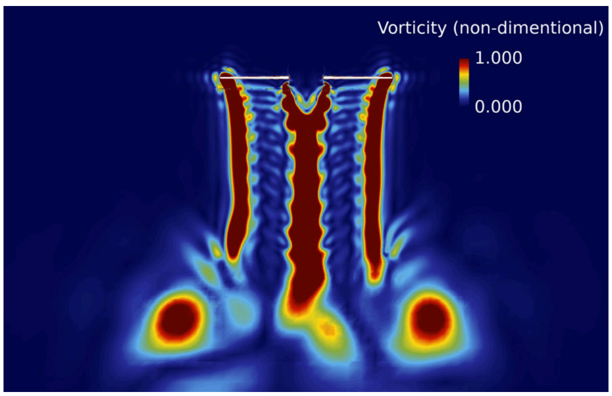

(a)

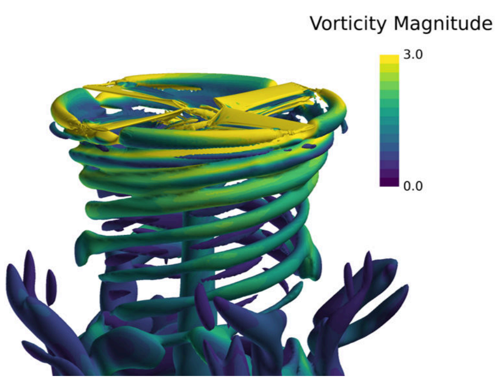

(b)

Fig. 9. CFD results for the ideally twisted rotor baseline case: (a) normalized vorticity magnitude in the vertical plane at the rotor center and (b) normalized iso-surface of Q-criterion colored by the vorticity magnitude

The measured thrust coefficient of the baseline case is 0.0123, which is 9.23% less than the target value designed with BEMT. Two possible explanations were provided by Pettingill *et al.* (Ref. 28) for this discrepancy. The first explanation describes that small errors in the collective pitch setup of the blade may affect the thrust. The second reason would be the inaccuracy of BEMT, especially due to tip loss effects. It is found that CFD underpredicts the measured thrust coefficient by 10.57%. This is similar to LBM-VLES results obtained by Thurman *et al.* (Ref. 23), where they underpredicted the thrust by 9.25% for the baseline ideally twisted rotor case. For our DDES case, blade pitch adjustment by 0.72° achieves the same thrust as the measurement. It is important to note that the margin of error in the blade pitch angle measurement provided by Pettingill (Ref. 28) is 0.4°.

Table 2 shows the predicted thrust for different meshes and collective pitches. Note that the second column listing the mesh follows the same numbering as Table 1. Cases 1, 3, and 5 of Table 2 are the meshes medium, fine, and extra fine meshes that only change in the near-body normal direction grid sizing. Despite increasing the mesh resolution, the thrust prediction did not improve, underpredicting by about 10% with $\theta_{tip} = 6.9°$. However, cases 2 and 4 show thrust-matched cases for the medium and fine mesh, respectively. The rationale for matching the thrust stems from the expectation that aligning the rotor's performance and aerodynamics with the experimental results would lead to more accurate predictions for the acoustic measurements. The effects that thrust had on acoustic measurements is discussed in a later section. The extra fine case with matching thrust was not simulated, as Table 2 already demonstrates good convergence, with results that do not vary significantly as the grid resolution increases.

Table 2. Ideally twisted rotor thrust predictions operating at 5500 RPM case with varying near-body mesh in the normal direction .

Case	Mesh	θ_{tip}	C_T	% Error
1	1	6.9°	0.0110	-10.57
2	1	7.62°	0.0122	-0.81
3	2	6.9°	0.0111	-9.76
4	2	7.62°	0.0123	0.00
5	3	6.9°	0.0111	-9.76

Table 3 shows the remaining meshes for the ideally twisted rotor baseline case. These cases are not pitched to match the thrust in order to align with the exact geometry described in Fig 1(a). Note that there is little to no change to the thrust predictions between the different cases shown. Case 7 in Table 3 is the coarsest mesh that is tested, yet it produces similar results to the fine mesh shown by Case 8. It is also important to note that the finer level 1 spacing in the O-B grid shown in Case 6 also has marginal differences.

Table 3. Ideally twisted rotor baseline with the predicted thrust coefficient and the error with varying near-body and off-body meshes.

Case	Mesh	Lvl 1 Size	C_T	% Error
1	1	10% C_{tip}	0.0110	-10.57
6	1	5% C_{tip}	0.0111	-9.76
7	4	10% C_{tip}	0.0110	-10.57
8	5	10% C_{tip}	0.0109	-11.38

Finally, Pettingill *et al* (Ref. 28) tested other tip angles at 5500 RPM. Those cases are also simulated, and their results are shown in Table 4. The rotor blades were pitched by negative or positive 3 degrees to achieve a tip angle of 3.9° and 9.9°. From the results shown in Tables 2 and 3, it is reasonable to use the baseline mesh to simulate the other tip angle cases. Thus, each case in Table 4 uses mesh 1 with a level 1 refinement of 10% C_{tip}. The prediction of the 3.9° case severely underpredicts the thrust at 5500 RPM. However, this is only about a 1 N underprediction. The other cases only underpredict by about 10%.

Table 4. Ideally twisted rotor at different tip pitches with the predicted thrust coefficient and error.

Case	θ_{tip}	C_T	% Error
1	6.9°	0.0110	-10.57
9	3.9°	0.0057	-27.80
10	9.9°	0.0161	-11.50

Approach 1 First, the trailing edge acoustic predictions are obtained using Approach 1, where the boundary layer parameters necessary to calculate the wall pressure spectrum are directly extracted from the CFD solution. Figure 10 shows the UCD-QuietFly prediction compared to the measurements made at microphone location 5 for the 5500 RPM and 6.9° tip angle case. The cases refer back to Table 2, where cases 1, 3, and 5 are the medium, fine, and extra fine near-body meshes that only varied in the normal direction. Each prediction captures the same trend as the experiment. They also predict the peak sound pressure level to occur at approximately 10-12 kHz, which UCD-QuietFly attributes to bluntness noise. Case 1, shown by the blue dashed line, underpredicts by about 5 dB below the peak frequency, while the finer Case 3 matches the experimental measurement better. However, Case 5 underpredicts the most despite having the finest mesh and predicting similar performance values. This opposing trend is attributed to the disadvantages of Approach 1, as it is highly sensitive to the locations where the boundary layer parameters are being extracted.

Exploring this issue further, the chordwise pressure gradient, which is one important input for noise prediction, is investigated along the rotor radius for the three mesh cases, as shown in Fig. 11. Note that each case has a large increase in pressure gradient near the tip. However, Case 5 has a significantly lower value near the tip compared to other cases. To verify that this is the source of the noise difference shown in Fig. 10, the pressure gradient was manually adjusted to match the value of Case 3. The results are shown in Fig. 12. It is confirmed that Case 5 with the altered pressure gradient yields a good match with Case 3. The small deviation between Case 3 and Case 5 (altered) is attributed to the remaining differences in other boundary layer parameters, whose impact is relatively insignificant.

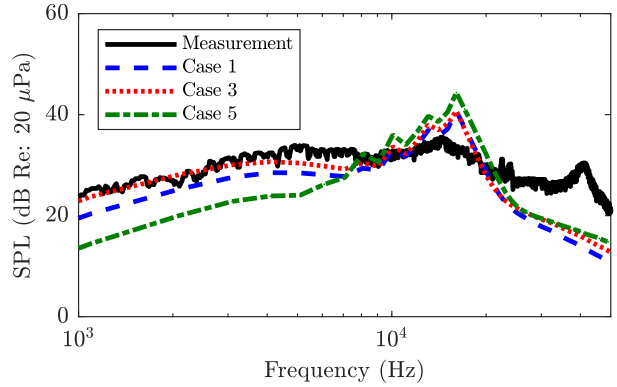

Fig. 10. Approach 1: UCD-QuietFly prediction for the ideally twisted rotor operating at 5500 RPM and $\theta_{tip} = 6.9°$.

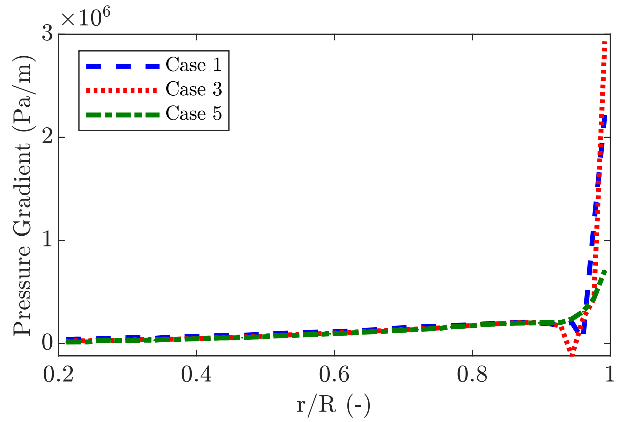

Fig. 11. Approach 1: Spanwise distribution of the trailing edge pressure gradient comparison

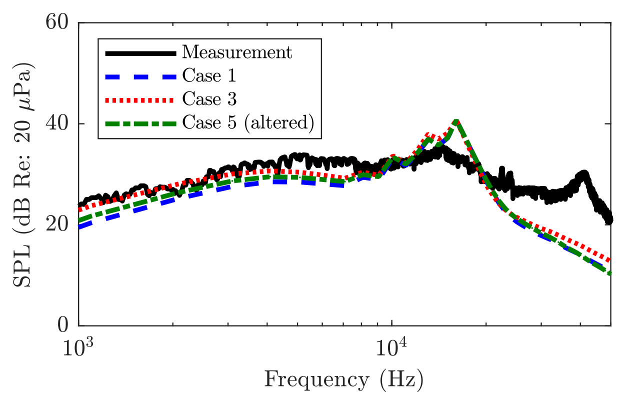

Fig. 12. Approach 1: UCD-QuietFly prediction for the ideally twisted rotor operating at 5500 RPM and $\theta_{tip} = 6.9°$ with altered pressure gradient for Case 5.

It is important to understand how this pressure gradient varies with mesh resolution or other CFD setup. Figure 13 shows the chordwise pressure gradient on the blade for the medium mesh at 5500 RPM and $\theta_{tip} = 6.9°$. It is shown that the pressure gradient exhibits rapid changes near the tip and trailing edge due to tip vortex interaction with the blade. This behavior is affected by the CFD mesh resolution. A minor change in the location, where the boundary layer parameters are extracted, even with the same mesh can lead to a large difference in noise due to the rapid change of the pressure gradient in magnitude in a small region. This is particularly important since the tip section is dominant in terms of noise generation. This tip vortex interaction also makes it difficult to choose the correct boundary layer thickness location due to the complex shape of the TKE or eddy viscosity as well as velocity profiles, as demonstrated in Fig 8.

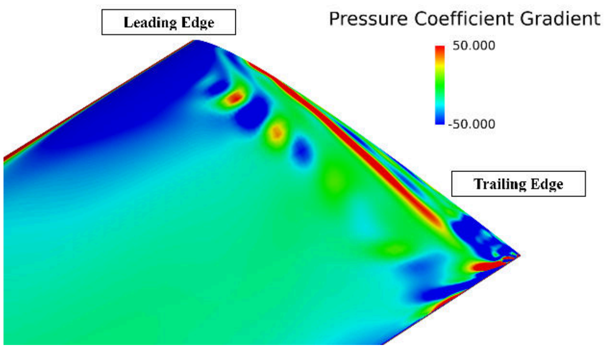

Fig. 13. Chordwise pressure coefficient gradient near the tip of the ideally twisted rotor.

A similar trend is observed when comparing the thrust-matched cases with different meshes in Cases 1-4, as shown in Table 2. It is expected that matching thrust would provide better acoustic results, and this is the case for the baseline mesh, as shown in Fig 14(a). However, despite the better prediction from the finer mesh in Case 3, the thrust-matched finer mesh (Case 4) underpredicts by 6 dB below the peak frequency. Similar to the previous example, this is attributed to the pressure gradient extracted at the tip. When the pressure gradient is manually adjusted, the prediction significantly improves, as seen in Fig 14(b), where Case 4 matches with Case 2 and Case 3.

Our investigation raises questions about the validity of Approach 1 due to its sensitivity to the boundary layer parameters, particularly when this approach is associated with the empirical wall pressure spectrum model as the input to the Amiet model. A similar conclusion was made by Jung *et al.* (Ref. 21) when they used the BPM model, but our study provides a more in-depth analysis of the issue when the Amiet model, in conjunction with the wall pressure spectrum model, is used to predict trailing-edge noise. Another important disadvantage of Approach 1 is the use of 3D flow data to obtain boundary layer values that are used in the 2D acoustic models. Therefore, it is necessary to consider alternative approaches that resolve the sensitivity issue and is more suitable for the acoustic models.

Approach 2 Approach 2, which involves using CFD and XFOIL, was described in the technical approach section. Figure 15 shows the results of using Approach 2 for Cases 1-4,

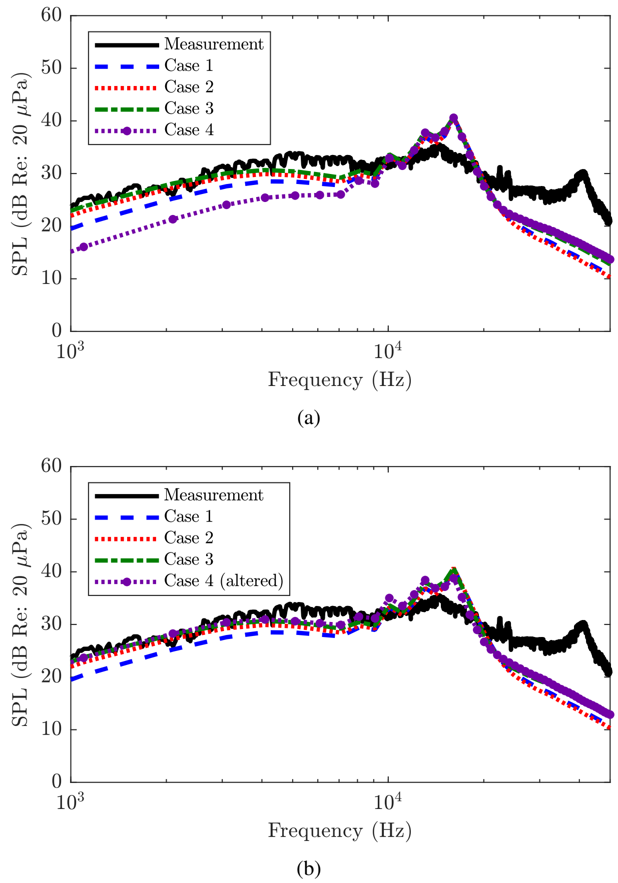

Fig. 14. Approach 1: UCD-QuietFly prediction for the ideally twisted rotor operating at 5500 RPM and $\theta_{tip} = 6.9°$, thrust matched.

where the sectional normal and chordwise forces are calculated from a CFD solution, and the boundary layer parameters are computed using XFOIL. The figure demonstrates that each case overlaps and matches both the trend and magnitude of the experimental data within 2 dB up to 20 kHz. It is found that Approach 2 is much less sensitive to mesh resolution and thrust matching compared to Approach 1. As long as the sectional normal and chordwise forces are similar for different CFD simulations, the boundary layer parameters are also similar, resulting in comparable acoustic results. This differs from Approach 1, where varying grid resolutions may change the eddy viscosity distribution, altering the placement of the boundary layer's edge, and the pressure gradient distributions near the tip.

It is interesting to observe that the acoustic results do not change with thrust matching (comparing Case 1 and 2 or Case 3 and 4). At first, this seems counter-intuitive since Approach 2 uses the blade's force distribution as input for obtaining the angle of attack distribution used to run XFOIL. To investigate this issue, we compare the effective angle of attack for Case 1 and Case 2. Figure 16 reveals a negligible increase in the effective angle of attack when thrust is matched. This is due to the increase in thrust not being significant, as the collective pitch is only increased by 0.72 degrees. Hence only a small in

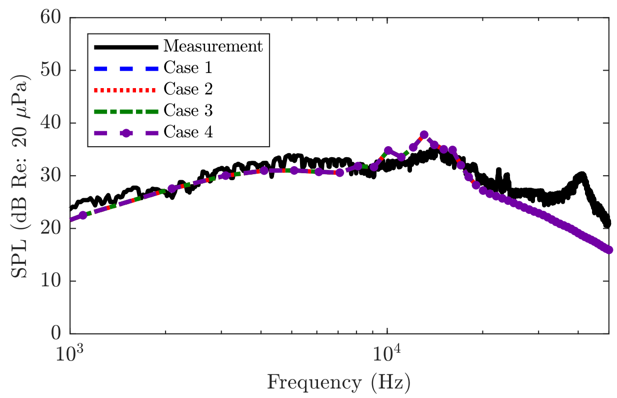

Fig. 15. Approach 2: UCD-QuietFly prediction for the ideally twisted rotor at 5500 rpm with $\theta_{tip} = 6.9°$.

the effective angle of attack distribution, resulting in XFOIL predicting similar boundary layer parameters. Owing to this lack of sensitivity, Fig 15 shows Cases 1-4 share almost the same values.

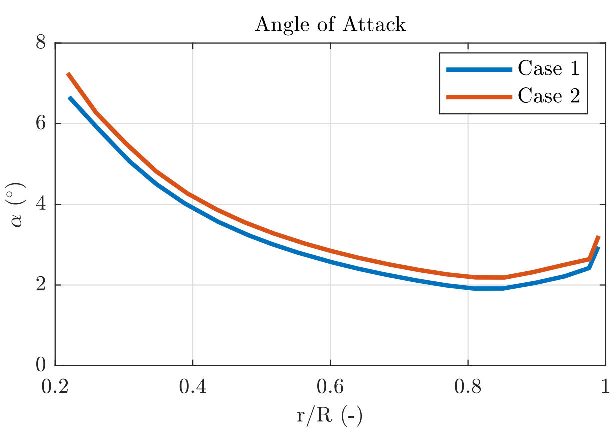

Fig. 16. Approach 2: ideally twisted rotor spanwise effective angle of attack distribution for Cases 1 and 2.

Figure 17 shows the directivity of overall sound pressure level (OASPL) to compare the predictions with measurement data at various microphone locations. Microphone locations are shown in Fig. 1(b). Case 1 is used in the prediction. The OASPL is calculated between 1 kHz and 10 kHz. It is seen that the microphone locations 2 and 5 match almost exactly the same as the measurements. Microphones 1 and 6 also only over-predict by about 1-2 dB. The least accurate prediction is at the $\theta = 0°$ location, where the OASPL is underpredicted by 10 dB. This is expected since the Amiet model results in cardinal noise directivity or significantly lower noise levels in the rotor plane. The measurement may also include some other broadband noise sources such as blade-wake interaction noise, which was not captured in the prediction.

Finally, the acoustic predictions for other tip angles are shown in Fig. 18(a) and 18(b). It is important to note that all three tip angles exhibit approximately the same magnitude for the sound pressure level in both the measured and predicted results. Observing this pattern provides evidence that thrust is not as significant a contributor to trailing edge noise as other parameters, such as rotation rate or airfoil geometry.

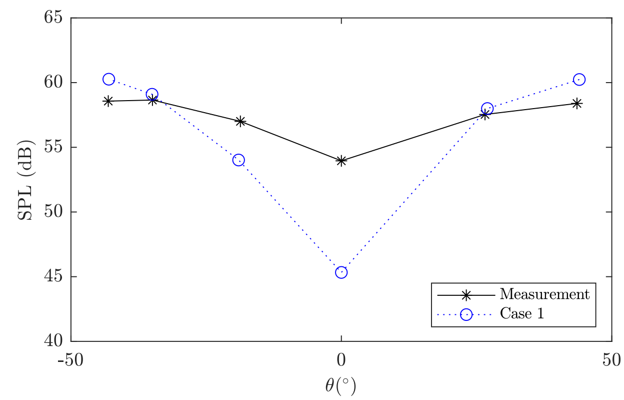

Fig. 17. Approach 2: OASPL directivity for the ideally twisted rotor (1-10kHz).

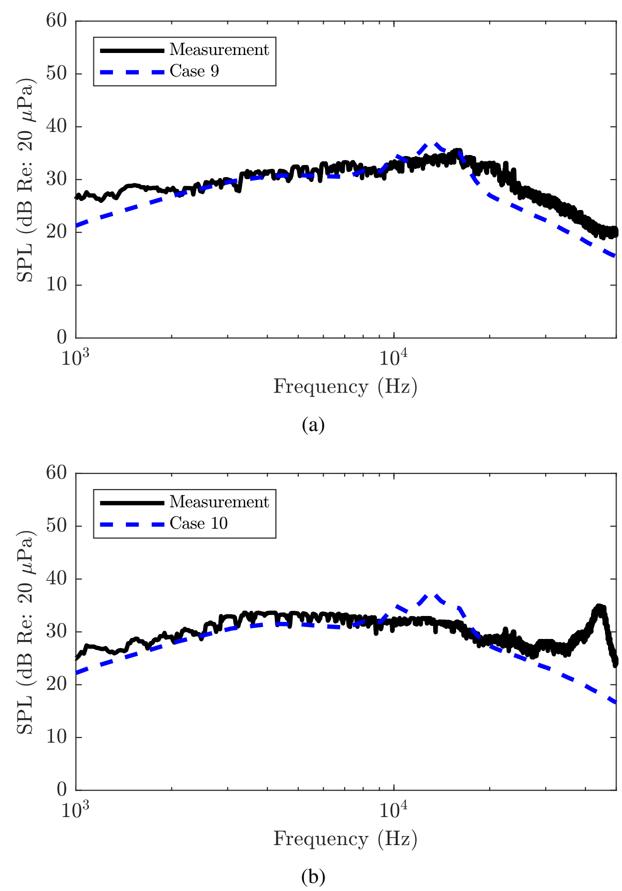

Fig. 18. Approach 2: UCD-QuietFly prediction for the ideally twisted rotor: (a) $\theta_{tip} = 3.9°$ and (b) $\theta_{tip} = 9.9°$.

Due to the consistency and accuracy achieved by Approach 2 with the ideally twisted rotor, the remaining results in this paper will utilize Approach 2.

SUI ROTOR

One of the motivations for investigating the SUI rotor is its utilization of multiple airfoils for each blade and its operation in forward flight. The ideally twisted rotor only employs a NACA 0012 airfoil, which simplifies the analysis; therefore, investigating more complex geometries is desirable. For the isolated forward flight cases, CFD underpredicts the thrust produced by rotor 1, achieving 9.33 N compared to the measured 10.85 N, yielding about 14% deviation. A similar discrepancy is observed for rotor 3, where CFD calculates a thrust of 14.26 N, while the experiment determined the thrust to be 15.72 N, which yields a 9.29% underprediction. This highlights the need for further refinement in modeling and meshes. However, the acoustic prediction could be less sensitive to the thrust value, as demonstrated earlier. Figure 19 shows the iso-surfaces of normalized Q-criterion of 0.1. The wake convection is well visualized in both cases.

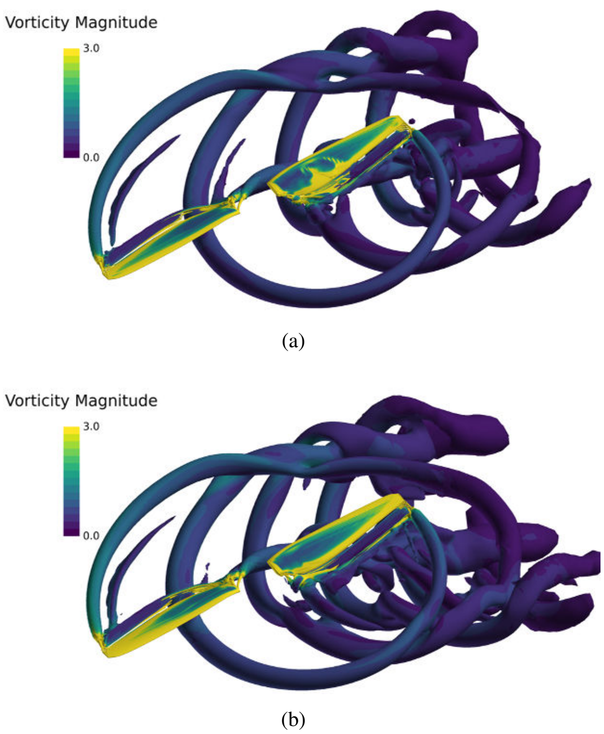

Fig. 19. SUI isolated rotor in forward flight iso-surfaces of Q-criterion colored by vorticity magnitude: (a) rotor 1 operating at 4000 RPM and (b) rotor 3 operating at 4900 RPM.

Using Approach 2, an angle of attack and velocity distributions are obtained and input into XFOIL within UCD-QuietFly. Figure 20 shows predicted and measure broadband noise levels for the rotor 1 and rotor 3 isolated forward flight cases, respectively. The "CFD/XFOIL" label represents the UCD-QuietFly prediction using Approach 2, as it employs both CFD and XFOIL to obtain the boundary layer parameters. The predictions align well with the experimental data near the noise peak at high frequencies for both cases. However, the predictions exhibit lower noise levels compared to the data at low frequencies. This discrepancy might be due to other broadband noise sources, such as blade wake interaction noise, which were not captured in the prediction. Interestingly, despite rotor 3 having a higher thrust and rotation rate, the 1/3 octave band sound pressure level is only slightly higher than that of rotor 1 for the frequencies of concern. This observation holds true for both the measurement and prediction values. The CFD predicts that rotor 1 has a maximum sound pressure level of 55 dB, while rotor 3 has a maximum of 56 dB. This small increase in sound pressure level suggests some dependence on rotation rate but also a high dependence on rotor geometry (i.e., airfoil selection and distribution), as both plots exhibit similar characteristics.

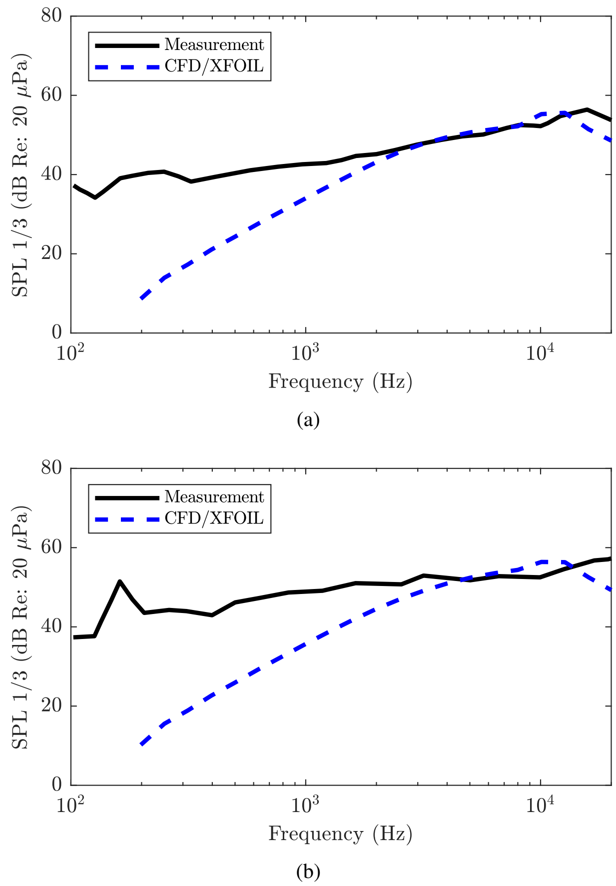

Fig. 20. SUI isolated rotor in forward flight broadband noise prediction: (a) rotor 1 operating at 4000 RPM and (b) rotor 3 operating at 4900 RPM.

MEJZLIK PROPELLER

Performance and tonal noise predictions for the Mejzlik propeller and wing cases are provided in a companion paper by Trembois *et al.* (Ref. 31). Although experimental data for comparison is unavailable, a brief examination of how the trailing edge noise of a propeller is influenced by the presence of a wing in its wake is conducted using UCD-QuietFly.

Figure 21 displays the vorticity contour on the vertical plane at the center of the nacelle, visualizing the propeller tip vortices and boundary layers on the wing and nacelle. At the top, the tip vortices are more contracted due to the wing's suction effect. Figure 22 shows the iso-surface of the normalized Q-criterion with the vorticity magnitude colored. The interaction between the propeller tip vortices and the wing leads to unsteady loading on the wing, which induces unsteady loading noise, as studied in detail by Trembois *et al.* (Ref. 31).

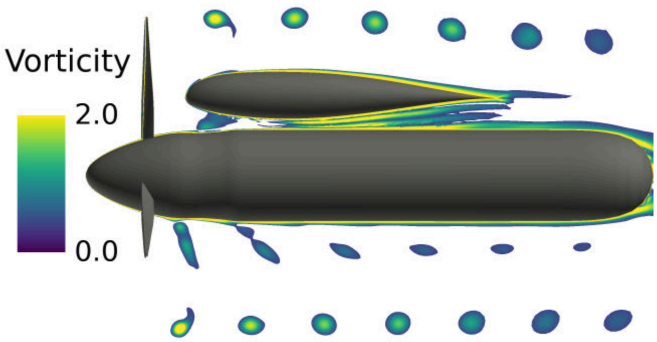

Fig. 21. Vorticity contours in the side view at the center of the propeller and wing (Ref. 31).

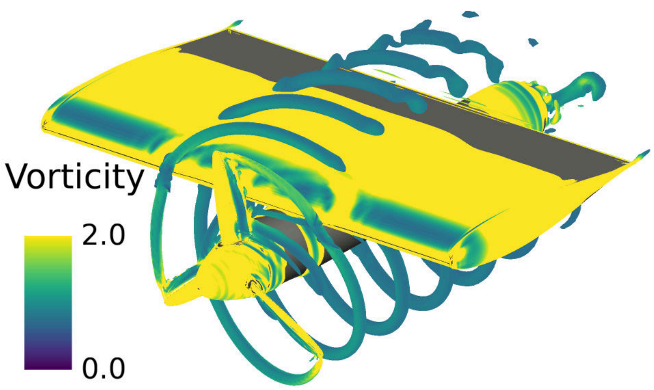

Fig. 22. Iso-surface of normalized Q-criterion with the vorticity magnitude colored (Ref. 31).

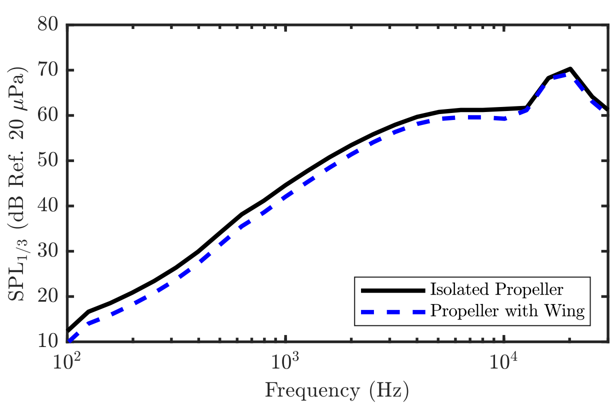

Fig. 23. Comparison of broadband noise between the isolated propeller and propeller with wing configurations.

Figure 23 presents the UCD-QuietFly prediction for the isolated propeller and the configuration where the wing is positioned 0.25 propeller radii behind the propeller blade leading edge and 0.5 radii above the propeller hub. Interestingly, the propeller-wing configuration is predicted to produce less noise than the isolated propeller. Between 100 Hz and 10 kHz, the propeller-wing configuration is predicted to have 2 dB less noise. The OASPL is also calculated using the frequency range of 1-10 kHz, resulting in 68.8 and 67.1 dB for the isolated propeller and propeller-wing cases, respectively.

The observed decrease in sound pressure level might be initially surprising, considering that the presence of the wing increases the propeller's thrust, which is associated with an increase in the effective angle of attack. However, the boundary layer thickness distribution shown in Fig 24 provides some justification for the lower sound pressure level. Figure 24(a) displays the boundary layer thickness as a function of radius for the lower surface of a propeller blade at a 0° azimuth angle, meaning the propeller blade is positioned vertically. The isolated propeller case exhibits a significantly higher boundary layer thickness throughout the radius, resulting in other boundary layer parameters being higher. For example, the displacement thicknesses on the lower surface for the propeller-wing configuration are much smaller than that for the isolated propeller, as seen in Fig 24(b). Figure 24(c) illustrates the pressure gradient at the trailing edge on the upper surface of the blade. It is worth noting that they are very similar, but the propeller with the wing exhibits slightly lower values in the inboard sections. Since the acoustic models depend on these factors, it follows that the propeller-wing configuration produces less noise. Note that we do not show all the parameters for the both upper and lower surfaces where the difference between the two cases are insignificant.

CONCLUSIONS

The prediction of broadband rotor noise using CFD is an evolving area of research, with various approaches and codes being developed. This paper investigates the application of the analytical Amiet model combined with Lee's wall pressure spectrum model. Lee's model necessitates information on the steady boundary layer near the trailing edge. As a result, RANS-based solvers in the form of hybrid LES and RANS (DDES) are employed in this study.

In this paper, two approaches were explored for utilizing CFD solutions in predicting rotor broadband noise. Approach 1 involves directly extracting boundary layer parameters, such as edge velocity, boundary layer thickness, displacement thickness, momentum thickness, chordwise pressure gradient, and friction coefficient, from the CFD flow data. While this method demonstrated some potential, with a few cases showing good agreement with experimental data, its high sensitivity to user-based inputs and grid resolution renders it impractical for general use. A more accurate and consistent approach is one that employs CFD to compute the force distribution on a rotor's blades and XFOIL to determine the boundary layer parameters. This approach exhibited low sensitivity to grid

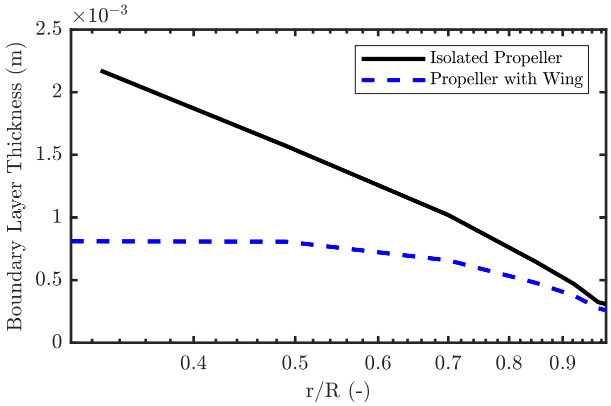

(a)

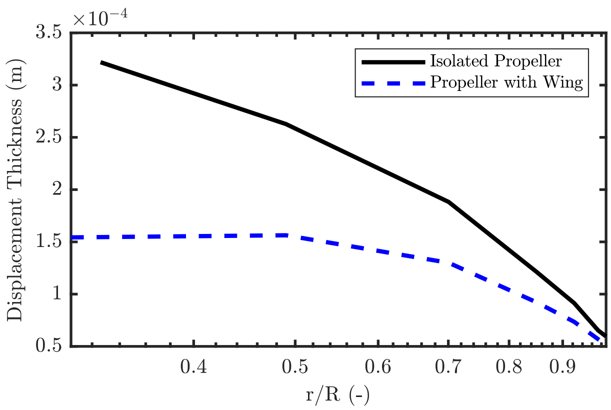

(b)

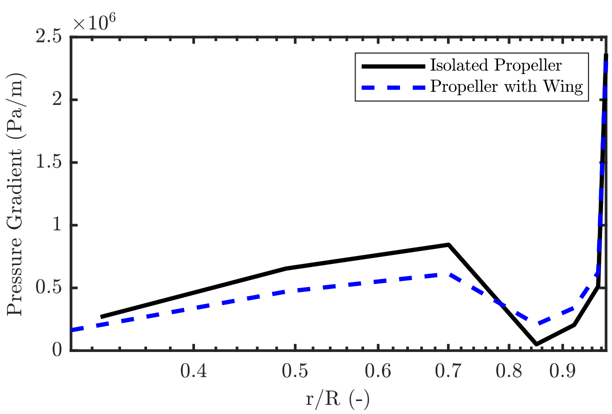

(c)

Fig. 24. Boundary layer parameters for the Mejzlik isolated propeller and propeller with wing: (a) lower surface boundary layer thickness, (b) lower surface displacement thickness, (c) upper surface pressure gradient.

size and thrust while aligning with the provided experimental data. The validation cases proved successful, as the ideally twisted rotor predictions deviated by only 1 dB between 1-20 kHz, and the SUI isolated rotor forward flight cases captured the high-frequency trend and magnitude between 3-12 kHz.

We also investigated the broadband noise generated by a propeller in combination with a wing for the first time. Interestingly, the broadband noise was reduced in the presence of the wing. Upon further examination, it was revealed that certain boundary layer parameters on the lower side of the propeller blades decreased when the wing was present. This suggests that the wing's interaction with the propeller could have a beneficial impact on noise reduction, warranting further investigation into the underlying mechanisms and potential applications. However, it should be noted that a wing itself could generate significant broadband noise, which was not accounted for in the current paper. Thus, the overall noise trend for the propeller-wing configuration should be further investigated.

Some observations from these validation cases indicate that the trend and magnitude of the sound pressure level appear to be primarily dependent on the airfoil shape and distribution in addition to the rotor's rotation rate. Interestingly, the thrust did not seem to affect predictions noticeably, as small changes in thrust had little to no impact on the effective angle of attack of a blade's 2D cross-section. Even with an increased angle of attack, a blade might produce less noise due to the airfoil generating favorable boundary layer values, as observed in the Mejzlik propeller and wing case.

Further research into identifying airfoil and blade shapes that reduce noise presents an intriguing future research topic. Ideally, the goal would be to discover airfoils that can deliver the same or better performance while generating less noise. This could contribute to the development of more efficient and quieter rotor systems for various applications. The Amiet model in conjunction with Lee's wall pressure spectrum model is believed to be suitable for this study since it can account for general airfoil shapes with camber.

ACKNOWLEDGMENTS

The authors appreciate the financial support from Supernal for UAM noise research. Special thanks to Dr. Yahia Ismail, Gregory Busch, and Dr. Shreekant Agrawal from Supernal for their invaluable discussions throughout this project. Resources supporting this work were partially provided by the NASA High-End Computing (HEC) Program through the NASA Advanced Supercomputing (NAS) Division at Ames Research Center.

REFERENCES

[1]Schäffer, B., Pieren, R., Heutschi, K., Wunderli, J., and Becker, S., "Drone Noise Emission Characteristics and Noise Effects on Humans - A Systematic Review," *International Journal of Environmental Research and Public Health*, Vol. 18, (11), pp. 5940.
doi: 10.3390/ijerph191811298

[2]Kim, J., "Urban Air Mobility Noise: Further Considerations on Indoor Space," *International Journal of Environmental Research and Public Health*, Vol. 19, (18), 2022, pp. 1–11.
doi: 10.3390/ijerph191811298

[3]Greenwood, E., Brentner, K. S., Rau, R. F., and Gan, Z. F. T., "Challenges and Opportunities for Low Noise Electric

Aircraft," *International Journal of Aeroacoustics*, Vol. 21, (5-7), 2022, pp. 315–381.
doi: 10.1177/1475472X221107377

[4]Sarojini, D., Ruh, M., Joshy, A., Yan, J., Ivanov, A., Scotzniovsky, L., Fletcher, A., Orndorff, N., Sperry, M., Gandarillas, V., Asher, I., Chambers, J., Gill, H., Lee, S., Cheng, Z., Rodrigues, G., Zhao, S., Mi, C., Nascenzi, T., Cuatt, T., Winter, T., Guibert, A., Cronk, A., Kim, H., Meng, S., and Hwang, J., "Large-Scale Multidisciplinary Design Optimization of an eVTOL Aircraft using Comprehensive Analysis," Proceedings of the AIAA SciTech Forum, National Harbor, MD, January 23–27, 2023, AIAA Paper 2023-0146.

[5]Orndorff, N., Sperry, M., Scotzniovsky, L., Gill, H., Sarojini, D., Hwang, J., Lee, S., Cheng, Z., Zhao, S., and Mi, C., "Air-taxi Transition Trajectory Optimization Using Physics-based Aerodynamic, Acoustic, and Motor Models," Proceedings of the AIAA SciTech Forum, National Harbor, MD, January 23–27, 2023, AIAA Paper 2023-0324.

[6]Brooks, T., Pope, D., and Marcolini, M., "Aifoil Self-Noise and Prediction," Technical Report NASA Reference Publication 1218, National Aeronautics and Space Administration, 1989.

[7]Lee, S., Ayton, L., Bertagnolio, F., Moreau, S., Chong, T. P., and Joseph, P., "Turbulent Boundary Layer Trailing-Edge Noise: Theory, Computation, Experiment, and Application," *Progress in Aerospace Sciences*, Vol. 126, 2021, pp. 100737.
doi: 10.1016/j.paerosci.2021.100737

[8]Wiener, N. and Hopf, E., "Über eine klasse singulärer integralgleichungen," *Sitzungsberichte der Preussischen Akademie der Wissenschaften, Physikalisch-Mathematische Klasse*, Vol. 31, 1931, pp. 696–706.

[9]Amiet, R., "Noise due to turbulent flow past a trailing edge," *Journal of Sound and Vibration*, Vol. 47, (3), 1976, pp. 387–393.
doi: 10.1016/0022-460X(76)90948-2

[10]Howe, M., "A review of the theory of trailing edge noise," *Journal of Sound and Vibration*, Vol. 61, (4), 1978, pp. 437–465.
doi: 10.1016/0022-460X(78)90391-7

[11]Roger, M. and Moreau, S., "Back-scattering correction and further extensions of Amiet's trailing-edge noise model. Part I: Theory," *Journal of Sound and Vibration*, Vol. 286, (3), 2005, pp. 477–506.
doi: 10.1016/j.jsv.2004.10.054

[12]Li, S. and Lee, S., "Predictions and Validations of Small-Scale Rotor Noise Using UCD-QuietFly," Proceedings of the Vertical Flight Society Technical Conference on Aeromechanics Design for Transformative Vertical Flight, January 25-27, 2022.

[13]Goody, M., "Empirical spectral model of surface pressure fluctuations," *AIAA Journal*, Vol. 42, (9), 2004, pp. 1788–1794.
doi: 10.2514/1.9433

[14]Lee, S., "Empirical Wall-Pressure Spectral Modeling for Zero and Adverse Pressure Gradient Flows," *AIAA Journal*, Vol. 56, (5), May 2018, pp. 1818–1829.
doi: 10.2514/1.J056528

[15]Lee, S. and Shum, J. G., "Prediction of Airfoil Trailing Edge Noise Using Empirical Wall Pressure Spectrum Models," *AIAA Journal*, Vol. 57, (3), 2019, pp. 888–897.
doi: 10.2514/1.J057787

[16]Brooks, T., Pope, S., and Marcolini, M., "Airfoil self-noise and prediction," Technical report, NASA Langley Research Center, Hampton, VA, 1989.

[17]Kang, D. and Lee, S., "Application of Wavelet Analysis to Trailing-Edge Noise," Proceedings of the 28th AIAA/CEAS Aeroacoustics Conference, Southampton, UK, June 14–17, 2022, AIAA Paper 2022-2891.

[18]Kang, D. and Lee, S., "On the Effect of Boundary-layer Tripping for Trailing-edge Noise Predictions," Proceedings of the AIAA SciTech Forum, National Harbor, MD, Jan 23–27, 2023, AIAA Paper 2023-0972.

[19]Li, S. and Lee, S., "Prediction of Rotorcraft Broadband Trailing-Edge Noise and Parameter Sensitivity Study," *Journal of the American Helicopter Society*, Vol. 65, (4), 2020, pp. 1–14.
doi: 10.4050/JAHS.65.042006

[20]Whelchel, J., Alexander, N., Pisharoti, N., Brizzolara, S., Murali, R., and Stilwell, D., "Examination of Broadband and Tonal Noise Sources Produced by eVTOL Propellers and Drive Systems," 28th AIAA CEAS Aeroacoustic 2022 Conference, June 2022.

[21]Jung Y., H. C., Baeder J., "Empirical Rotor Broadband Noise Prediction Using CFD Boundary Layer Parameter Extraction," *Journal of the American Helicopter Society*, Vol. 68, (032010), 2023.
doi: 10.4050/JAHS.68.032010

[22]Thurman, C., Zawodny, N., and Baeder, J., "Computational Prediction of Broadband Noise from a Representative Small Unmanned Aerial System Rotor," 76th Annual Forum & Technology Display, October 2020.

[23]Thurman, C., Zawodny, N., Pettingill, N., Lopes, L., and Baeder, J., "Physics-Informed Broadband Noise Source Identification and Prediction of an Ideally Twisted Rotor," AIAA Scitech 2021 Forum, January 11–15 & 19–21, 2021.

[24]Zawodny, N., Boyd, D., and Burley, C., "Acoustic Characterization and Prediction of Representative, Small-Scale Rotary-Wing Unmanned Aircraft System Component," American Helicopter Society (AHS) Annual Forum, May 17–19, 2016.

[25]Thai, A., De Paola, E., Di Marco, A., Stoica, L., Camussi, R., Tron, R., and Grace, S., "Experimental and Computational Aeroacoustic Investigation of Small Rotor Interactions in Hover," *Applied Sciences*, Vol. 11, (21), 2021, pp. 10016.
doi: 10.3390/app112110016

[26]Li, S. and Lee, S., "Prediction of Urban Air Mobility Multirotor VTOL Broadband Noise Using UCD-QuietFly," *Journal of the American Helicopter Society*, Vol. 66, (3), 2021, pp. 1–13.
doi: 10.4050/JAHS.66.032004

[27]Li, S. and Lee, S., "Acoustic Analysis and Sound Quality Assessment of a Quiet Helicopter for Air Taxi Operations," *Journal of the American Helicopter Society*, Vol. 67, (3), 2022, pp. 1–15.
doi: 10.4050/JAHS.67.032001

[28]Pettingill, N., Zawondny, N., Thurman, C., and Lopes, L., "Acoustic and Performance Characteristics of an Ideally Twisted Rotor in Hover," AIAA Scitech 2021 Forum, January 11–15 & 19–21, 2021.

[29]Pettingill, N. and Zawondny, N., "Identification and Prediction of Broadband Noise for a Small Quadcopter," Vertical Flight Society 75th Annual Forum Technology Display, May 13–16, 2019.

[30]Zawodny, N. S., Boyd, D. D., and Nark, D. M., "Aerodynamic and Acoustic Interactions Associated with Inboard Propeller-Wing Configurations," AIAA Scitech 2021 Forum, Virtual, January 19–21, 2021.

[31]Trembois, N., Lee, S., Ramsarran, T., and Brentner, K., "Prediction of Interactional Aerodynamic Noise of Propellers and Wing Using High-Fidelity CFD," Proceedings of the 79th Annual Forum of the Vertical Flight Society, May 16–18, 2023.

[32]Trembois, N. P., *Automatic Mesh Generation of Structured Overset Rotor Blades*, Master's thesis, University of California, Davis, Davis, CA, December 2020.

[33]Nichols, R. and Buning, P., *User's Manual for OVERFLOW 2.2*, NASA Langley Research Center, Hampton, Virginia, August 2010.

[34]Nichols, R., Tramel, R., and Buning, P., "Solver and Turbulence Model Upgrades to OVERFLOW 2 for Unsteady and High-Speed Flow Applications," AIAA Paper 2006-2824, 25th AIAA Applied Aerodynamics Conference, San Fransisco, California, June 5–8, 2006.

[35]Jia, Z. and Lee, S., "Aerodynamically Induced Noise of a Lift-Offset Coaxial Rotor with Pitch Attitude in High-Speed Forward Flight," *Journal of Sound and Vibration*, Vol. 491, 2021, pp. 115737.

[36]Jia, Z. and Lee, S., "Computational Study on Noise of Urban Air Mobility Quadrotor Aircraft," *Journal of the American Helicopter Society*, Vol. 67, 2022, pp. 012009.

[37]Jia, Z. and Lee, S., "High-Fidelity Computational Analysis on the Noise of a Side-by-Side Hybrid VTOL Aircraft," *Journal of the American Helicopter Society*, Vol. 67, (2), 2022, pp. 022005.

[38]Drela, M., "XFOIL: An Analysis and Design System for Low Reynolds Number Airfoils," *Low Reynolds Number Aerodynamics*, edited by T. J. Mueller, Vol. 54, Springer, Berlin, Heidelberg, 1997.

[39]Gill, H. and Lee, S., "Effect of 2D Ice Accretion on Turbulent Boundary Layer and Trailing-Edge Noise," *International Journal of Aeroacoustics*, Vol. 21, (3-4), 2022, pp. 260–285.